International Journal of Heat and Fluid Flow 29 (2008) 820–829

Contents lists available at ScienceDirect

International Journal of Heat and Fluid Flow

journal homepage: www.elsevier.com/locate/ijhff

Turbulence structural measurements using a comprehensive laser–Doppler velocimeter in two- and three-dimensional turbulent boundary layers ☆

K. Todd Lowe *, Roger L. Simpson

Department of Aerospace and Ocean Engineering, Virginia Tech, 215 Randolph Hall, Blacksburg, VA 24061, USA

ARTICLE INFO

Article history:
Received 9 November 2007
Received in revised form 4 March 2008
Accepted 8 March 2008
Available online 22 April 2008

Keywords:
Turbulence structure
Dissipation rate
Velocity–pressure gradient correlation
Reynolds stress transport
Laser–Doppler velocimetry/anemometry
Turbulent boundary layers

ABSTRACT

The advanced 'comprehensive' laser–Doppler velocimeter is used to acquire spatially and temporally resolved turbulence structural measurements in high Reynolds number two- and three-dimensional turbulent boundary layers. The new instrument directly measures three-dimensional particle trajectories at high repetitions. These trajectories are analyzed in post-processing to obtain fluctuating velocity gradient tensor fields, which lead to direct measurements of turbulent viscous dissipation rates. Such data acquired in two- and three-dimensional boundary layers with an approach flow momentum thickness Reynolds number, $Re_\theta = 7500$ are presented. Results indicate that anisotropy of the dissipation rate of Reynolds stresses persists to similar heights in viscous wall units as obtained with direct numerical simulations at lower Reynolds numbers. Measurements in a three-dimensional turbulent boundary layer in the vicinity of a wing/body junction also indicate that a reduction in the value of the velocity/pressure-gradient correlations for the Reynolds normal stresses reduces the turbulent energy redistribution and contributes to reduced shear stress magnitudes, as observed previously through DNS (Moin, P., Shih, T.-H., Driver, D., Mansour, N.N., 1990. Direct numerical simulation of a three-dimensional turbulent boundary layer, Phys. Fluids A 2 (10), 1846–1853).

1. Introduction

In this paper we present measurements of non-isotropic dissipation rates and velocity–pressure gradient correlations obtained in two- and three-dimensional turbulent boundary layers using an optical technique that shares its fundamental attributes with the convention laser–Doppler velocimetry technique. Direct measurements of the nine-component velocity gradient tensor are achieved by measuring the velocity and position of seed particles arriving in a small measurement volume in rapid succession, extrapolating their trajectories over short time periods, and determining the velocity gradient field that is most-consistent with the velocities and positions of the particles observed. The details of the technique just mentioned are discussed to follow, but first the motivations for developing a new optical technique to obtain the nine-component velocity gradient tensor is explained.

Understanding turbulence transport in shear flows is a key topic in fundamental research due to the immediate implications that the Reynolds stress transport equations have on modeling for the Reynolds stresses. Although the most-obvious uses for the models of the turbulence structural (transport) terms is in Reynolds-averaged Navier–Stokes (RANS) solutions, other solution techniques benefit from the information obtained by studying Reynolds-averaged turbulence structure. For instance, hybrid LES/RANS approaches have been developed and shown to be much more computationally efficient than LES and produce promising results (Labourasse and Sagaut, 2002).

The Reynolds stress transport equations are given as

$$\frac{D\overline{u_i u_j}}{Dt} = P_{ij} + \Pi_{ij} + \nu\nabla^2\overline{u_i u_j} - \varepsilon_{ij} - \frac{\partial\overline{u_i u_j u_k}}{\partial x_k} \tag{1}$$

where the production rate of the Reynolds stress tensor, $\overline{u_i u_j}$, is $P_{ij} = -\overline{u_i u_k}\partial\overline{U_j}/\partial x_k - \overline{u_j u_k}\partial\overline{U_i}/\partial x_k$, the velocity–pressure-gradient tensor is $\Pi_{ij} = -(1/\rho)\overline{u_i(\partial p/\partial x_j) + u_j(\partial p/\partial x_i)}$ with p being the fluctuating static pressure, the dissipation-rate tensor is $\varepsilon_{ij} = 2\nu\overline{(\partial u_i/\partial x_k)(\partial u_j/\partial x_k)}$, and ν is the kinematic viscosity. Each of the terms with the exception of Π_{ij} in Eq. (1) may be measured using the 'comprehensive' laser–Doppler velocimeter (CompLDV) described by Lowe (2006) and Lowe and Simpson (in preparation). To obtain transport rate budgets, Π_{ij} is determined by the balance of Eq. (1) using direct measurements for each of the terms therein, including the non-isotropic dissipation rate tensor, ε_{ij}. The dissipation rate tensor is directly evaluated from velocity gradient

☆ Manuscript submitted to the International Journal of Heat and Fluid Flow for inclusion in the special issue for the 5th International Symposium on Turbulence and Shear Flow Phenomena.

* Corresponding author. Present address: Applied University Research, Inc., 605 Preston Avenue, Blacksburg, VA 24060, USA. Tel.: +1 540 797 0643; fax: +1 866 223 8673.
E-mail address: toddlowe@aurinc.com (K. Todd Lowe).

0142-727X/$ - see front matter © 2008 Elsevier Inc. All rights reserved.
doi:10.1016/j.ijheatfluidflow.2008.03.003

measurements that are possible with the unique capabilities of the CompLDV to be discussed.

By determining the non-isotropic dissipation rate directly and without the use of Taylor's Hypothesis and anisotropy models, a higher fidelity measurement of the velocity–pressure gradient tensor, Π_{ij}, is possible in high Reynolds number flows that cannot be simulated by direct numerical simulations (DNS). The importance of the velocity–pressure gradient term in wall-bounded three-dimensional (3D) flows has been shown for low Reynolds numbers by the DNS of Coleman et al. (2000). In the strained channel flow DNS, those authors discovered that Π_{ij} is of primary importance to the evolution of the Reynolds stresses. They showed that the lag between the mean shear rate and the Reynolds shear stresses, a key modeling problem in 3D flows, is primarily due to this term. Understanding the role of the velocity–pressure-gradient tensor in redistributing the Reynolds stresses is a key to improved modeling for the future of RANS and hybrid LES/RANS approaches.

The direct measurement of velocity gradients for determining non-isotropic dissipation rates has received much attention in experimental fluid mechanics, due to the fundamental need for such measurements. Several researchers have utilized a number of techniques for making turbulent velocity gradient measurements, such as hot-wire anemometry (Wallace and Foss, 1995), particle image velocimetry (Meneveau and Katz, 2000; Mullin and Dahm, 2006), and laser–Doppler velocimetry (LDV; Tarau et al., 2002; Yao et al., 2001; Agui and Andreopoulos, 2002). The reader is referred to Lowe (2006) for a more extensive review of the prior art in velocity gradient measurements. All the prior methods examined for turbulent velocity gradient measurements suffer from significant limits in spatial resolution and/or velocity dynamic range and are of limited applicability to high Reynolds number flows. This void is partially filled by the new CompLDV technologies discussed herein.

2. The comprehensive LDV technique

The CompLDV technique is capable of making highly resolved particle trajectory measurements in turbulent flows (Lowe, 2006; Lowe and Simpson, in preparation). The technique is based upon the principles of Gaussian beam coherent laser interference and Doppler shift due to scattering by particles seeding a test flow so that the instrument is closely related to the LDV technique. The CompLDV employs a novel optical arrangement to achieve low-uncertainty, time-resolved measurements of three-components each of particle position, velocity, and acceleration. In this work, the use of such measurements for directly estimating velocity gradients is explored.

In past work, sub-measurement volume position resolution LDV techniques have been developed (Czarske, 2001; Czarske et al., 2002). These methods employ interference fringe patterns with calibrated spatial variations to obtain particle position resolutions at two-orders of magnitude smaller scales than the measurement volume diameter.

The method may be understood examining the Doppler equation for differential LDV

$$U_{\perp} = f_D d \tag{2}$$

where $U_{\perp}$ is the velocity of the particle perpendicular to the fringes, f_D is the Doppler frequency and d is the interference fringe spacing. Now consider the case when two parallel measurement volumes with varying fringe spacing profiles are overlapped, as depicted schematically in Fig. 1 where a hypothetical set of fringes diverges while an overlapping set converges along the bisector axis of the laser beams, the ratio of the Doppler equations for the two systems becomes

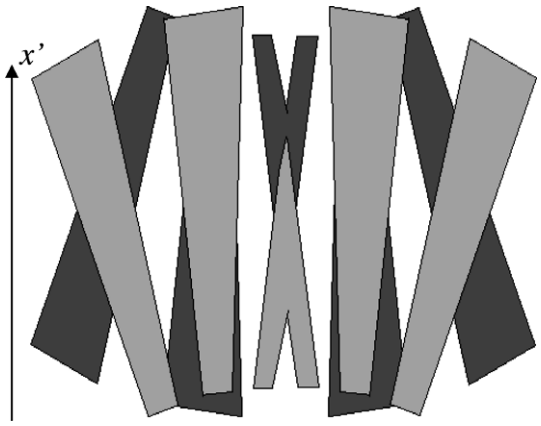

Fig. 1. Schematic of overlapping fringe sets with varying fringe spacings along the measurement volume beam-bisector.

$$\frac{U_1}{U_2} = \frac{f_{D1} d_1}{f_{D2} d_2} = 1 \tag{3}$$

since $U_1 = U_2$ for parallel measurement volumes. It follows then that:

$$\frac{f_{D1}}{f_{D2}} = \frac{d_2}{d_1} \tag{4}$$

Now if the fringe spacing is non-uniform along the measurement volume, then the ratio of the two Doppler frequencies is a function of the crossing position within the measurement volume. Also, if the fringe spacings vary monotonically along the measurement volume, as is the case if one set of fringes are converging while the other is diverging as illustrated schematically in Fig. 1, there will exist a monotonic function, q, such that

$$\frac{f_2}{f_1} = \frac{d_1(x'_{\text{cross}})}{d_2(x'_{\text{cross}})} = q(x'_{\text{cross}}) \tag{5}$$

where x'_{cross} is the particle crossing position measured axially along the measurement volume. The function $q(x')$ is a property of a given beam alignment and may be calibrated by measuring the fringe spacing along the measurement volume. Using the instantaneous measurements of the Doppler frequency ratios, the calibration may be interpolated to find the particle crossing position.

The key development for measuring velocity gradients with this technique is the capability to measure positions of successively arriving particles at very high spatial resolution in three spatial dimensions. This same fundamental concept is used in the CompLDV and described further by Lowe (2006) and Lowe and Simpson (in preparation), where CompLDV-specific system principles and operation are discussed. The current system is optimized for making velocity gradient measurements by giving low uncertainties in velocity and position in three linearly independent directions; typical single sample uncertainties at 95% confidence are 0.2% of the velocity magnitude for each of three velocity components, about 4 μm in the stream-wise position, and 10 μm in both directions in the secondary flow plane (independent of the flow velocity, Lowe and Simpson, in preparation).

2.1. Instrumentation details

The optical probe hardware for the CompLDV includes precision optics and alignment hardware for both laser transmitting and scattered-light receiving systems. Laser light from a 5W argon-ion laser (Coherent Innova I90C-5) operating in multi-line mode is conditioned on an optical table before being transmitted via fiber optics to the probe. The collimated light from

each polarization-maintaining fiber optic passes through independent focusing achromatic lenses housed within the CompLDV probe hardware, focusing the beams into a single measurement volume. A pair of achromatic lenses acting at a magnification of one-half gathers scattered light from the measurement volume and couples it into a multimode fiber with a 100 μm diameter core. A side-view photograph of the fiber optic probe is given in Fig. 2.

The light gathered by the receiving optics exits the multimode optical fiber and travels through chromatic separation optics before being measured by photomultiplier tubes. Acquisition of the photomultiplier signals is controlled using a standard personal computer with an eight-bit, 250 MSample/s PCI digitizer. A custom signal processing suite is used to extract burst information. The signal processing modules include burst recognition and envelope estimation algorithms, frequency domain processing, and burst validation. These algorithms have been validated using model burst signals with noise as described by Lowe (2006) and Lowe and Simpson (2007). Burst detection is accomplished by estimating the signal envelope by obtaining time-local root-mean-square (RMS) signal values; a parabolic fit to the logarithm of every five local RMS values was used along with the value of the local RMS to determine when and where Gaussian-windowed bursts were present. For signal snippets in which bursts were detected and centered in the time-window, the Doppler frequencies were estimated using the burst spectral distribution computed with the fast Fourier transform (FFT) by interpolating the Doppler peak using three-point Gaussian interpolation (Shinpaugh et al., 1992). Signal validation parameters, including the ratios of the primary Doppler peak power to the secondary spectral peak power and the narrowband signal-to-noise ratio (Shinpaugh et al., 1992), are recorded along with Doppler frequency information.

2.2. Proof-of-concept measurements

To exhibit the capabilities of the CompLDV for particle position measurement, velocity profile measurements in two-dimensional (2D) flat plate TBLs are presented in Fig. 3. These data have been obtained in the Department of Aerospace and Ocean Engineering Boundary Layer Research Wind Tunnel at Virginia Tech. CompLDV measurements at two momentum thickness Reynolds numbers

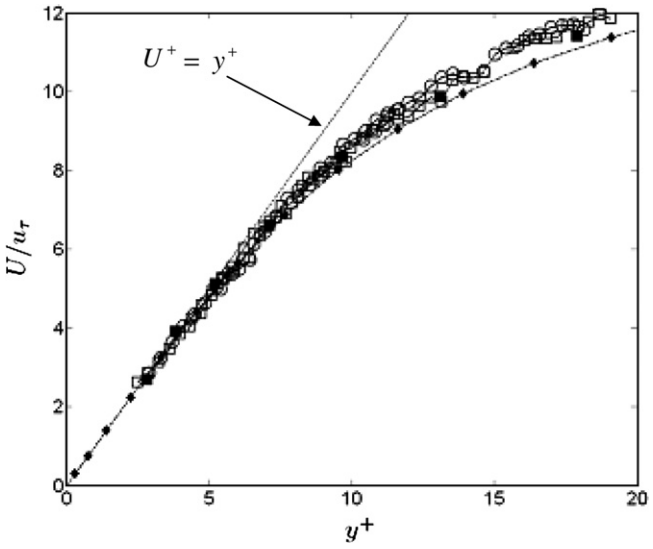

Fig. 3. Resolved profiles for the mean stream-wise velocity in viscous wall scaling. □, current data for $Re_\theta = 5930$; ○, current data for $Re_\theta = 7500$; ■, LDV data of DeGraaff and Eaton (2000) for $Re_\theta = 5160$.◇, DNS data of Spalart (1988) for $Re_\theta = 1410$. The dashed line in this plot is the viscous sublayer relationship, $U^+ = y^+$.

($Re_\theta \equiv U_\infty \theta / \nu$, where θ is the momentum thickness), $Re_\theta = 5930$ and $Re_\theta = 7500$ are plotted. For these data, the tunnel free-stream velocity was set at $U_\infty = 27.95$ m/s for the greater Reynolds number and $U_\infty = 21.00$ m/s for the lesser, while the tunnel temperature was always $T = 25\ ^\circ\text{C} \pm 0.5\ ^\circ\text{C}$. Measurements were acquired at six individual positions of the center of the measurement volume relative to the wall. The data presented are the mean stream-wise velocity statistics that have been divided among bins according to the normal-to-wall particle positions measured relative to the measurement volume center. When the profile data are normalized with viscous wall scaling using the skin friction velocity, u_τ, as the velocity scale and the viscous length scale to normalize the vertical height, $y^+ \equiv y/\delta_\nu = y u_\tau/\nu$, the comparison with previous conventional LDV data of DeGraaff and Eaton (2000) at a comparable Reynolds number along with the DNS data of Spalart (1988) at

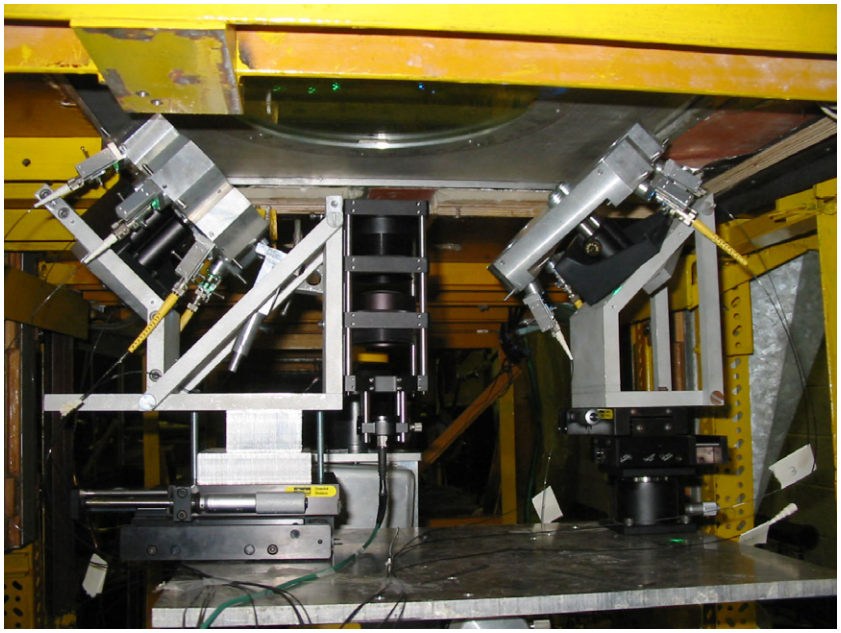

Fig. 2. Photograph of CompLDV probe hardware.

a lower Reynolds number is excellent, particularly in the viscous sublayer.

2.3. Velocity gradient measurement concept

The temporally and spatially resolved measurements of seed particle velocity and position obtained using the CompLDV may be extended to particle *trajectory* measurements by expanding the trajectory, $\vec{r}(t)$, around the particle arrival time, t_A, through a Taylor series expansion. The advantage to such an expansion in this case is that the point-wise measurements of the particle parameters at the measurement volume center may be extended within truncation limits forward and backward in time and space. The result is an effective extended measurement volume, as shown in Fig. 4 for the trajectory of a single particle, which may span several diameters of the laser measurement volume in which direct measurements are made. It is upon this principle that the velocity gradient measurement concept relies.

The problem of estimating velocity gradients from CompLDV trajectory data is posed as follows:

> Given the velocities and relative positions of N particles ($N \geqslant 4$), determine the velocity gradient tensor that is consistent with the data within experimental uncertainties and the constraints imposed by coherent turbulence scales.

The geometry of the problem is shown schematically in Fig. 5. The particles arrive randomly in space and time. The statistics of the arrivals depends on the turbulence level as well as the velocity gradients across the volume (Albrecht et al., 2003). In the case of zero turbulence and velocity gradient, the arrival time statistics follow a Poisson (exponential) distribution, while the particles are uniformly distributed in space. The probability density function of the measurement volume validation weights the arrival position so that the measured positions are not uniformly distributed. The extrapolated volume, as depicted in Fig. 5, is aligned approximately with the mean flow direction in the case that turbulent flow angles are relatively small.

A technique for estimating the velocity gradients from CompLDV data is developed based upon an over-constrained system for the N particles that cross the measurement volume within the allowable time t. To construct a least-squares cost function, some model for the distribution of the measured quantities must be assumed. In this case, we desired a coherent-structure-based model for the velocity field observed over a short record of time. The model adopted is based upon a generic swirling structure

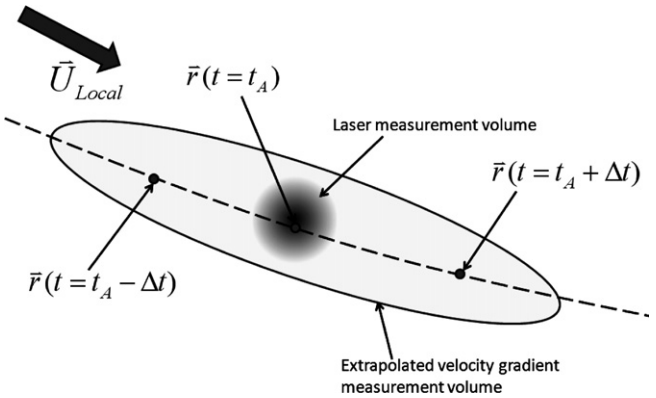

Fig. 4. Schematic illustration of the trajectory of a single particle at the particle arrival time, t_A as well as the extrapolated times $t_A \pm \Delta t$. The direct measurement (velocity and position at time t_A) is made within the laser measurement volume, while velocity gradients are estimated using the extrapolated measurement volume.

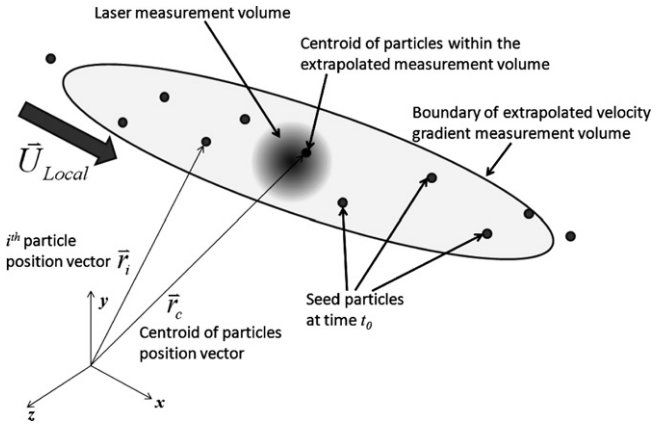

Fig. 5. Schematic of an instance for the CompLDV extrapolated measurement volume containing several particles (represented by small circles) with measured velocities and positions. Symbols defined in text.

aligned with the nominal mean flow direction and with a relatively large extent in space for that direction. The near-wall coherent structures in the 2DFPTBL such as the quasi-stream-wise vortex of Robinson (1991) have been observed as dominant features, and these structures are consistent with the current model. Further from the wall, it is still observed that the stream-wise 'legs' of 'crescent-shaped' structures are those that contribute to dissipation of the turbulence energy in the Reynolds stresses as the legs stretch and the vorticity within is intensified (Robinson, 1991). The existence of these elongated dissipative structures gives credence to a technique that utilizes a long-narrow region of fluid as the basis for obtaining resolved velocity gradients. A simple structure of the velocity distribution is assumed such that the nine Cartesian-components of the velocity gradient tensor are modeled as constant within the observed region of flow.

To implement the model chosen, we refer again to Fig. 5. The centroid velocity and position of the N particles may be readily obtained from the measured Doppler data. In the case that the velocity field assumed is exact and the measurements are without uncertainty, then a velocity gradient field which is consistent with the measurements obtained according to the model (i.e., velocity gradients are constant within the measurement region) will result in the following exact relationship:

$$(U,V,W)_i = (U,V,W)_c + [(\vec{r}_i - \vec{r}_c)\cdot\vec{\nabla}](U,V,W)_c \tag{6}$$

where $\vec{r}_i$ is the position vector of the ith particle, $\vec{U}_i = U_i\hat{i} + V_i\hat{j} + W_i\hat{k}$ is the velocity vector of the ith particle, $\vec{r}_c$ is the position vector of the centroid location of the N particles considered for velocity gradient tensor estimation, and $\vec{U}_c = U_c\hat{i} + V_c\hat{j} + W_c\hat{k}$ is the centroid velocity vector ($U_c = \sum_{i=1}^{N} U_i |\vec{r}_i - \vec{r}_c| / \sum_{i=1}^{N} |\vec{r}_i - \vec{r}_c|$) for the N particles. Eq. (6) may also be thought of as the 3D Taylor-series expansions for the velocity components truncated for velocity derivatives of order 2 and greater [although one may refine velocity estimates using the CompLDV acceleration measurements to enhance the order of the method (Lowe and Simpson, 2006)].

In the CompLDV measurements, uncertainty exists both for the measurements obtained as well as for the model equations (6). To mitigate this, redundant measurements for several particles are used along with Eq. (6) to construct objective cost functions that must be minimized by successive guesses for the velocity-gradient tensor. The cost function chosen is a least-squares error function developed from Eq. (6):

$$\Phi_{U,V,W} = \sum_{i=1}^{N} \{(U,V,W)_c + [(\vec{r}_i - \vec{r}_c)\cdot\vec{\nabla}](U,V,W)_c - (U,V,W)_i\}^2 \tag{7}$$

where $\Phi_{U,V,W}$ represents the three cost functions that are minimized to obtain the velocity gradient estimates. In the current implementation, the particle velocities, $(U,V,W)_i$, are taken as constant as the particle convects within the extended measurement volume. Note that in this implementation, the velocity components are decoupled except in the convection velocities that are hidden in the calculation of the particle position vectors:

$$\vec{r}_i(t=t_0) = U_i(t_0 - t_A)\hat{i} + [y_i + V_i(t_0 - t_A)]\hat{j} + [z_i + W_i(t_0 - t_A)]\hat{k} \quad (8)$$

where t_A is the arrival time for the ith particle, t_0 is the time at which the centroid information is computed, and y_i and z_i are the position components directly measured by the CompLDV within the laser measurement volume. It is taken that the arrival time measurement for the burst occurs when the particle is at the location $x_i = 0$, which is an excellent assertion considering the potential relative uncertainties when compared with the overall length of the extended measurement volume under consideration.

The least-squares velocity gradient technique just described was tested for computational and statistical robustness using a Monte Carlo simulation to ensure that the optimization scheme would return the proper velocity gradient tensor with no uncertainties input. In this simulation, particle inter-arrival times were sampled from the exponential Poisson distribution with a mean particle rate of 20,000 particle arrivals per time unit. A representative point at $y^+ = 100$ in the 2D flat-plate turbulent boundary layer was used for mean velocities and mean velocity gradients as given in Table 1, but no turbulence was input. In Table 1, the symbol δ indicates the 95% confidence uncertainty in the quantity that follows, as used for sampling that quantity in the Monte Carlo simulation. Simulations with 6 and 7 particles used in the least-squares optimization were carried out. It is reiterated, that no turbulence is entered either within the velocities or the gradients – all deviations from zero-variance are due to uncertainties in the gradient scheme and inherent measurement uncertainties. The resulting statistics indicate that the mean velocity gradient input was recovered with less than 5% discrepancy, while the artificial turbulence levels, indicative of fluctuating gradient uncertainties, were on the order of $\delta(\overline{\partial u_i/\partial x_j)^2}^+ < 3\times10^{-4}$ at 95% confidence (where the superscript + indicates viscous wall scaling). For relative comparison, typical values in the 2DFPTBL at $y^+ = 100$ for the mean-square fluctuation tensor are $\overline{(\partial u_i/\partial x_j)^2}^+ \approx 0.003 - 0.006$ with the exception of the stream-wise velocity gradient along the same direction which is smaller, $O(0.001)$. Since the x-position is measured at such a small *relative* uncertainty (see the extended measurement volume geometry in Fig. 5), the artificial stream-wise velocity gradients fluctuations were observed from the simulation to be $\delta(\overline{\partial u_i/\partial x)^2}^+ < 4\times10^{-7}$ at 95% confidence, indicating that the complete tensor could be measured at acceptable uncertainty levels.

It is appropriate at this point to discuss some of the limitations of the velocity gradient technique described above. Due to the nature of the position estimation technique, it is not possible to obtain un-biased estimates of particle position as the mean velocity approaches zero relative to the root-mean-square (RMS) velocity fluctuations. This arises due to large turbulent velocities that exist in the secondary flow directions, resulting in signal chirps that broaden the Doppler spectra and increase the Doppler frequency uncertainties to relative levels that prevent position estimates (Lowe, 2006; Lowe and Simpson, in preparation). In regions of small mean velocity relative to the RMS of the turbulent velocity fluctuations, the coherent structures that exist will also fail to have the same characteristics of those known to exist in attached boundary layers due to the fundamental change in the shear flow necessary for a region of low relative mean velocity compared with RMS velocities. Despite this limitation that includes regions near separating boundary layers and recirculating regions, the impact possible for difficult-to-predict 3D boundary layers is substantial. It is to this end of improving the understanding of attached 3D turbulent boundary layers that the key results to be presented are focused.

Table 1
Input parameters for the uncertainty simulations for the least-squares velocity gradient estimation method at $Re_\theta = 7500$ and $y^+ = 100$

U (m/s)	$\overline{\frac{\partial U}{\partial y}}$ (s^{-1})	δx (μm)	$\delta y, \delta z$ (μm)	$\delta U, \delta V, \delta W$	Data rate (kHz)
16.25	1478.2	4	10	0.38% of $\|\vec{U}\|$	20

To implement the velocity gradient measurement scheme discussed above, time windows for accepting series of particles were determined based upon prior work in determining coherent structure convection velocities and sizes. For the coherent structures in the near-wall region, it has been observed that the convective speed of coherent eddies is approximately constant when scaled upon the wall friction velocity, $U_C/u_\tau \approx 14$ (Ahn and Simpson, 1987), and typical active near-wall structures exist in very long dimensions of $x^+ = 500$ or greater (Robinson, 1991). Time windows were specified that were always less than the ratio of the stream-wise length scale to the convective velocity scale. In practice, this model for obtaining the velocity gradients requires some adaptation. First, it has been found that the variances of the stream-wise velocity gradients measured [those that are obtained using the arrival time technique for determining the positions, i.e., $\overline{(\partial(U,V,W)/\partial x)^2}$] are much too small when such a time-window is allowed, while the secondary-direction gradients $[\overline{(\partial(U,V,W)/\partial y)^2}, \overline{(\partial(U,V,W)/\partial z)^2}]$ are correctly measured with the above time window guideline (time window, $t^+ = 35$). Due to the intrinsic shape of the extrapolated measurement volume, the span-wise and normal-to-wall gradients are estimated over comparatively small-distances in those directions, although these measurements extend across a significant stream-wise region. A possible explanation for the attenuation of gradients measured in the stream-wise direction is the manifestation of the requirement to obtain velocity gradient measurements at resolutions approaching the Kolmogorov length scale. Such a requirement is satisfied for the transverse directions (due to the elongation of the extended measurement volume), albeit while requiring stationarity of the velocity gradients in those directions within the coherent structure. On the other hand, the small-scale stream-wise fluctuations within the coherent structures appear to vary along the long structure; and as such, a time-window of $t^+ = 6$, shorter than the $t^+ = 35$ guideline above, is used to obtain stream-wise gradients, resulting in a capture of the small-scale stream-wise fluctuations. An example of the results for the stream-wise gradient estimation is given in Fig. 6, where (isotropic) spectral dissipation rate estimates are compared to the directly estimated mean-square of the stream-wise gradient of the stream-wise velocity and to the turbulent kinetic energy (TKE) production computed from Reynolds-averaged profile measurements in a 2DFPTBL at $Re_\theta = 5930$ (Lowe, 2006). The comparison of the two TKE dissipation rate measurements to the production measurements rests on the assumption of the isotropic relation, $\varepsilon = 15\nu\overline{(\frac{\partial u}{\partial x})^2}$ and the observation/assertion that TKE production and dissipation rates balance throughout some region of the boundary layer; but the direct comparison of the two estimates of dissipation rate to one-another is more rigorous since the spectral fitting discussed above seeks to directly estimate the term $\overline{(\frac{\partial u}{\partial x})^2}$ via Taylor's hypothesis. The quality of the comparison for these two measurements of $\overline{(\frac{\partial u}{\partial x})^2}$ gives confidence in the gradient estimation scheme for stream-wise gradients.

In contrast to the stream-wise gradients, span-wise and normal-to-wall gradients measured with the scheme exhibit noise-limited values as the real velocity gradient variances approach small values. The approach for correcting the variance values in

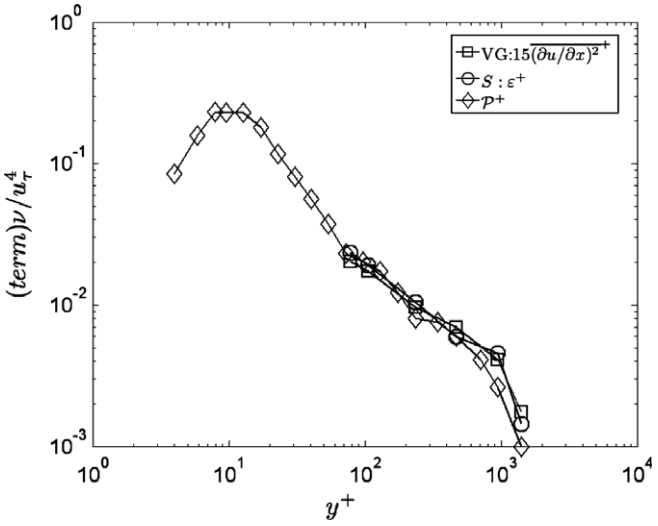

Fig. 6. Comparison of the dissipation estimate for the directly estimated stream-wise velocity gradient in the stream-wise direction to the spectral dissipation rate estimates and the production for the 2DFPTBL at $Re_\theta = 5930$. VG, directly estimated dissipation rate from velocity gradients; S, spectral-estimates of dissipation rate and Diamonds are TKE production computed from Reynolds-averaged statistics.

the presence of noise is to apply a constant subtractive correction to the terms $(\partial(U,V,W)/\partial y)^2, (\partial(U,V,W)/\partial z)^2$. The premise for applying such a correction is that it is a white-noise floor that limits the minimum variance for these velocity gradients; and the variance of this noise is most closely related to the variance in particle position estimates – which is independent of velocity magnitude (Lowe, 2006; Lowe and Simpson, in preparation). The dissipation rate data presented to follow has been corrected by subtracting constant noise-floor variance values from each of the velocity gradient variance terms used in the calculation (with the exception of the stream-wise gradient terms as discussed above). The goal in selecting these noise-floor values was to obtain mean-square velocity gradient estimates of the same order of magnitude as the stream-wise gradients for the transverse direction gradients in the outer-portion of the boundary layer where conditions approach those needed for assuming local isotropy (Saddoughi and Veeravalli, 1994).

3. Results and discussion

The technique for obtaining dissipation rate measurements was applied to the 2DFPTBL at $Re_\theta = 7500$ and a 3D TBL alongside of a wing/body junction undergoing the same approach flow as the flat plate case in the Turbulent Boundary Layer Research Wind Tunnel mentioned in Section 2. For both flows, the approach flow was carefully adjusted to achieve a zero-pressure gradient with a free-stream velocity of $U_\infty = 27.95$ m/s, and all measurements were taken at a tunnel temperature of $T = 25\ ^\circ\text{C} \pm 0.5\ ^\circ\text{C}$. The flow parameters for the 2DFPTBL are given in Table 2. Aerosol particle seeding for the measurements was generated by vaporizing a Dioctyl Phthalate aerosol and allowing it to re-condense in a duct before injecting this seed into the boundary layer of the approach flow. The vaporization/condensation process results in a more uniform diameter seeding with particle diameter distributions in the range $0.54\ \mu\text{m} < d_p < 0.68\ \mu\text{m}$. These particle diameters result in less than 3 dB of attenuation in Lagrangian velocity fluctuations at frequencies up to 160 kHz using the first-order particle lag model (Lehmann et al., 2002) – sufficient for resolving all the meaningful scales of motion.

The skin friction velocity results given in Table 2 were determined by fitting the sublayer data of Fig. 3 to the rigorous viscous sublayer equations that are derived using the unsteady continuity equation and the momentum equation (Rotta, 1962; Tang, 2004; Durst et al., 1995)

$$\begin{aligned} U &= \frac{\tau_{wx}}{\mu}y + \frac{1}{2\mu}\frac{\partial P}{\partial x}\Big)_{\text{wall}} y^2 + C_U y^4 \\ W &= \frac{\tau_{wz}}{\mu}y + \frac{1}{2\mu}\frac{\partial P}{\partial z}\Big)_{\text{wall}} y^2 + C_W y^4 \end{aligned} \tag{9}$$

where U and W are mean velocities in the plane parallel to the wall, μ is the dynamic viscosity of the fluid, $\frac{\partial P}{\partial x})_{\text{wall}}$ and $\frac{\partial P}{\partial z})_{\text{wall}}$ are the wall pressure gradients, $C_U = \frac{1}{24\nu}\frac{\partial^3(\overline{uv})}{\partial y^3}|_{y=y_{\text{wall}}}$, and $C_W = \frac{1}{24\nu}\frac{\partial^3(\overline{vw})}{\partial y^3}\Big|_{y=y_{\text{wall}}}$. Here τ_{wx}, τ_{wz}, C_U and C_W were obtained from the mean velocity profile curve fits.

The near-wall polynomial velocity profile is observed to yield reliable shear stress estimates for $y^+ < 9$ [Tang (2004)], so that several points from Fig. 3 could be used to estimate the skin friction velocity.

The distributions of the Reynolds normal stress dissipation rates measured with the velocity gradient technique are plotted in Fig. 7, normalized using wall variables. To the authors' knowledge, these measurements are the first of their kind at Reynolds numbers of this magnitude in turbulent boundary layers. The measurements in the $Re_\theta = 7500$ flow closely follow the trends of the DNS data of Spalart (1988) at $Re_\theta = 1410$. Note that anisotropy exists in the dissipation rate to values of y^+ of about 100, similar to the results obtained by Ölçmen and Simpson (1996) using the anisotropy model of Hallbäck et al. (1990) for the same flow. These results contradict simple blending function models such as the one due to Lai and So (1990), which gives isotropic predictions for $y^+ > 10$.

Using the dissipation rate data from Fig. 7 and the velocity statistics data from the measurements, Eq. (1) may be used to extract the Π_{ij} profile. By balancing the Reynolds stress transport equations to obtain the velocity–pressure gradient correlation, several terms contribute to the uncertainty in the results for Π_{ij}. Examining the uncertainties for each of the terms quickly reveals that the dominant uncertainty is in the dissipation rate measurements, and the velocity–pressure gradient uncertainty is thus very nearly equal to the uncertainty in the dissipation rate measurements. A battery of experiments using the current instrumentation has indicated a noise floor in the mean squares of velocity gradients with a value of $\delta(\frac{\partial u_i}{\partial x_j})^2\frac{\nu}{u_\tau^4} \approx 0.003$. Although it is possible that further post-processing may be used to estimate the velocity gradient fluctuation auto-covariance more precisely in the presence of noise, the measured noise floor value above is proposed as a conservative estimate for the fluctuating velocity gradient uncertainty. Since three mean-square values are used to compute normal stress dissipation rates [e.g., $\varepsilon_{11} = \left(\frac{\partial u_1}{\partial x_1}\right)^2 + \left(\frac{\partial u_1}{\partial x_2}\right)^2 + \left(\frac{\partial u_1}{\partial x_3}\right)^2$], then the uncertainty in the velocity–pressure gradient correlation may be taken as equal to the dissipation rate uncertainty, $\delta\varepsilon_{ij} = \delta\Pi_{ij} =$

Table 2
Flow parameters for the $Re_\theta = 7500$, 2D flat-plate turbulent boundary layer reported

Re_θ	U_∞ (m/s)	u_τ (m/s)	δ, boundary layer thickness (mm)	θ (mm)	δ^*, displacement thickness (mm)	$H \equiv \delta^*/\theta$	δ_ν (μm)
7500	27.95	1.022	39.0	4.46	6.00	1.345	16.1

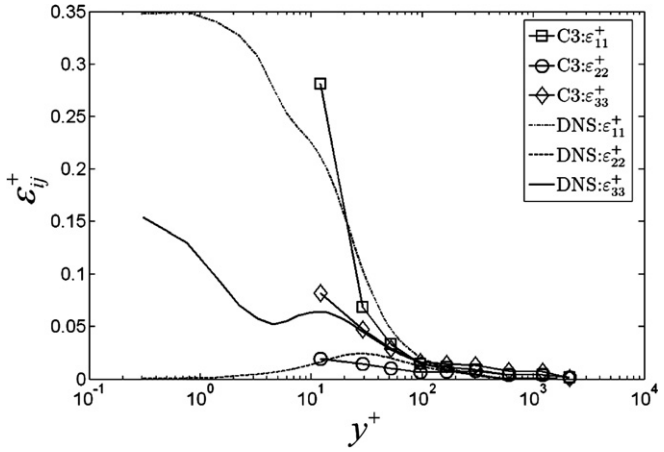

Fig. 7. Non-isotropic Reynolds stress dissipation rate in the 2DFPTBL. C3, CompLDV data for $Re_\theta = 7500$; DNS, simulation data of Spalart (1988) for $Re_\theta = 1410$.

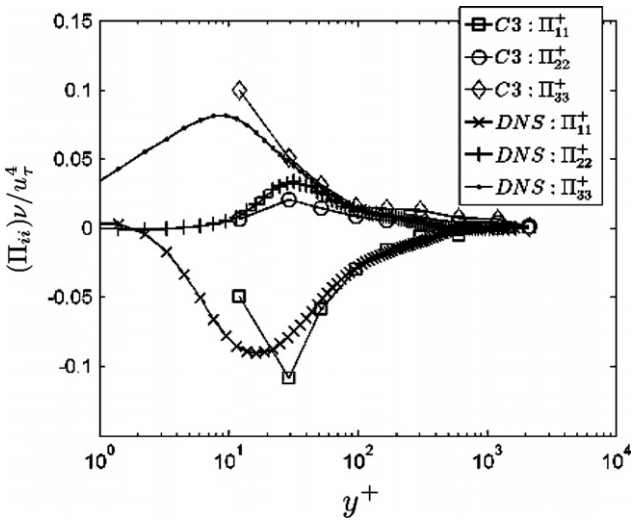

Fig. 9. Velocity/pressure gradient correlation in the 2DFPTBL at $Re_\theta = 7500$. C3, CompLDV and DNS, simulation data of Spalart (1988).

$\sqrt{3}\delta(\overline{\frac{\partial u_i}{\partial x_j}})^2$, so that the final uncertainty in the current measurements for the velocity–pressure gradient term in wall units is $\delta\Pi_{ij}\frac{\nu}{u_\tau^4} = 0.01$at 20:1 odds.

The normal stress velocity–pressure gradient terms are plotted in Fig. 9 for the $Re_\theta = 7500$ 2DFPTBL in comparison with the DNS results of Spalart (1988) for $Re_\theta = 1410$. While it is very difficult to validate such measurements due to the lack of information that exists for Π_{ij} at high Reynolds numbers, the similarity of the data to the wall-normalized DNS data gives confidence in the technique. Note that no profile smoothing has been used to obtain the results plotted.

Of even greater interest than the 2D case, the 3D attached turbulent boundary layer in the vicinity of a wing/body junction has been measured using the CompLDV. The geometry of the wing, depicted schematically in Fig. 8, is a 3:2 elliptical nose joined at the maximum thickness to a NACA 0020 airfoil with a maximum thickness of 7.17 cm. The wing spans approximately 90% of the test section height, creating a pressure-driven three-dimensional turbulent boundary layer on the bottom floor of the facility [Fig. 8(b)]. This particular flow was well-studied at Virginia Tech (Devenport and Simpson, 1990; Ölçmen and Simpson, 1995; Simpson, 2001). The complex flow includes a chaotic separated region very near the junction of the wing, a highly unsteady horseshoe vortex that is formed at the leading edge of the wing/body junction, and span-wise pressure gradients that generate stream-wise vorticity and strong three-dimensionality.

The present CompLDV data were acquired at a location reported in previous works under the designation of 'station 5', which is located outside the horseshoe vortex at $x/t = 0.026$, $z/t = -2.94$, where x is in the stream-wise direction and z is in the span-wise direction, both measured from the leading edge of the wing, and t is the maximum thickness of the wing. At this station, detailed, low-uncertainty conventional three-component LDV data exist (Ölçmen and Simpson, 1995, 1996). For consistency, the current data are compared with those of Ölçmen and Simpson in Figs. 10–13. Note that the data in Figs. 10, 12 and 13 were reduced as volume-averaged statistics such that the effective measurement volume diameter for them was about 100 μm. The mean velocities in this particular boundary layer profile are given in Figs. 10 and 11 with comparisons between present data and those of Ölçmen and Simpson in both cases. The presentation of data in Fig. 11 is directly analogous to those measurements in the 2DFPTBL in Fig. 3, where several y-positions of data are obtained for single measurement volume positions by separating measurements into bins according to particle y-position data. Clearly, the multi-velocity-component operation of the CompLDV is seen therein, and these data were used to determine the skin friction velocity via a fit to the coplanar velocity gradient (Tang, 2004) to be $u_\tau = 1.20$ m/s, which compares favorably within uncertainties with the value

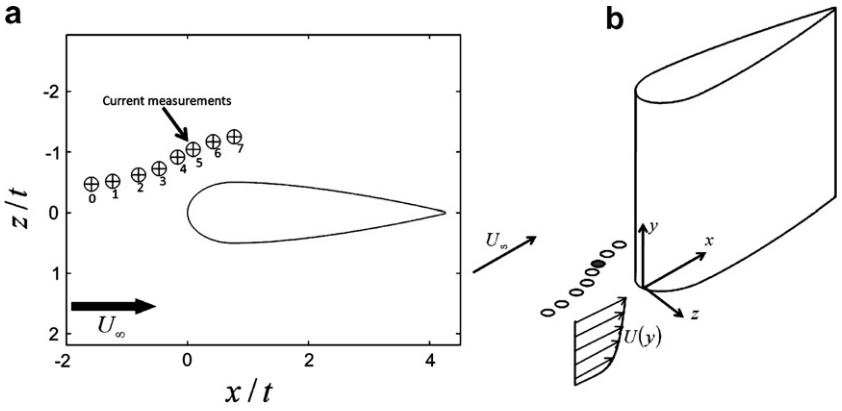

Fig. 8. Wing/body junction geometry and configuration for the 3D TBL measurements. (a) Top-view of the geometry of the wing/body junction flow studied; numbered symbols indicate previously studied measurement 'station' nomenclature. (b) Perspective view. The filled circle indicates the location of station 5 where current measurements are reported.

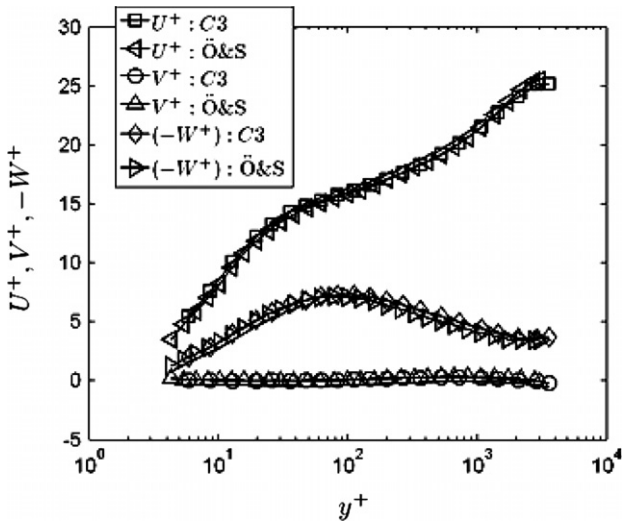

Fig. 10. Mean velocities for the wing/body junction flow at station 5. C3, CompLDV; Ö&S, Ölçmen and Simpson (1995). 'Tunnel' coordinate system x-axis is aligned with the inflow velocity vector and y-axis is normal-to-wall.

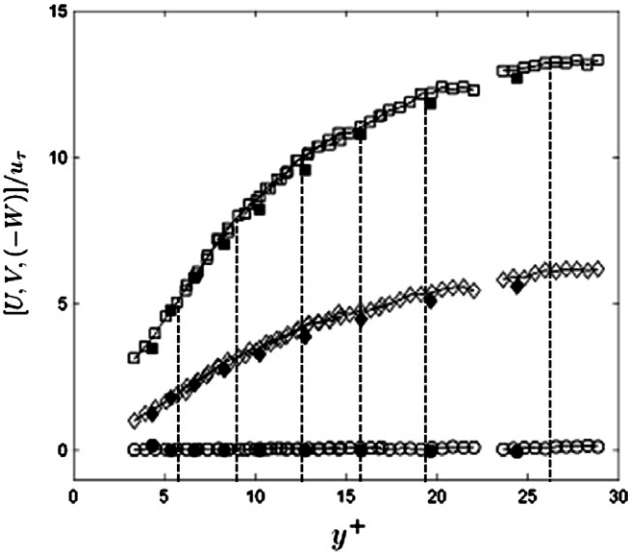

Fig. 11. Sub-measurement volume resolution mean velocities for the wing/body junction flow at station 5. Symbols: □, $\overline{U}/u_\tau$; ○, $\overline{V}/u_\tau$; ◇, $-\overline{W}/u_\tau$. Open symbols are current CompLDV measurements; solid symbols are data of Ölçmen and Simpson (1995). Vertical dashed lines show center locations of measurement volume. Tunnel coordinate system.

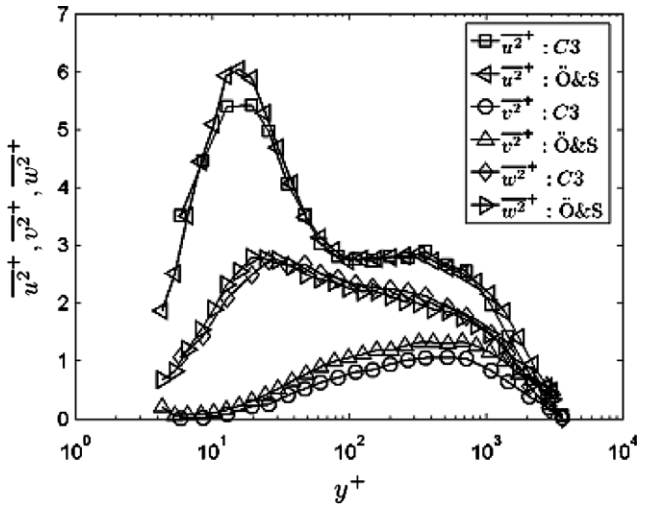

Fig. 12. Reynolds normal stresses for the wing/body junction flow at station 5. C3: CompLDV; Ö& S: Ölçmen and Simpson (1995). Tunnel coordinate system.

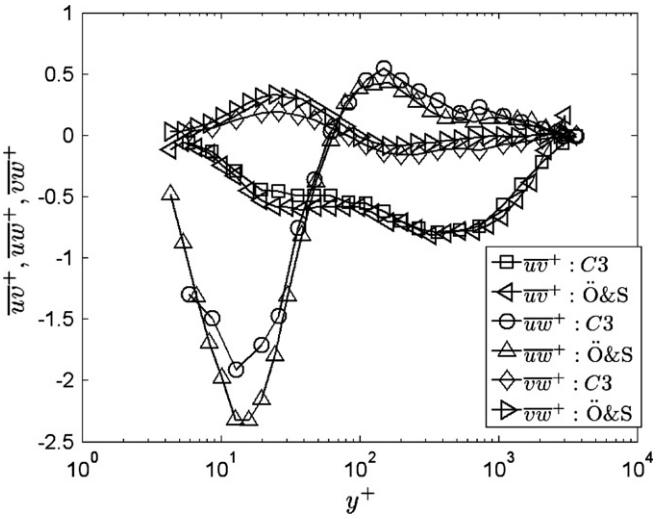

Fig. 13. Reynolds shear stresses for the wing/body junction flow at station 5. C3, CompLDV; Ö&S, Ölçmen and Simpson (1995). Tunnel coordinate system.

determined by Ölçmen and Simpson of $u_\tau = 1.15$ m/s. In Figs. 12 and 13, the Reynolds normal and shear stresses corrected for velocity gradient broadening (Durst et al., 1995) are compared with the results of Ölçmen and Simpson and indicate that the flow conditions were faithfully repeated in the currently reported experiment.

The dissipation rate measurement technique has been applied to the data for the wing/body junction flow. The transport rate budgets were computed using these non-isotropic dissipation rates and are presented in Fig. 14. The boundary layer form of the Reynolds stress transport equations was considered in obtaining the transport budgets such that only vertical gradients of Reynolds-averaged terms were computed. Eq. (1) was balanced using the non-isotropic dissipation rates to obtain the measurements of the velocity–pressure gradient correlations, Π_{ij}.

As noted by many previous authors, there is a reduction in the near-wall TKE and Reynolds shear stress for a wide array of 3D TBLs and correspondingly in the TKE and shear stress production, the present flow included (Simpson, 2005; Coleman et al., 2000; Moin et al., 1990; Ölçmen and Simpson, 1996; Eaton, 1995). In the present data, reduction of the near-wall TKE and Reynolds shear stress production (not plotted) is accompanied by reduced values of Π_{ii} compared with the 2DFPTBL (Fig. 15). This same result has been observed by Moin et al. (1990) through DNS. Those authors postulated that the reduction of shear stresses in their pressure-driven 3D wall-bounded flow was due to mechanisms that suppressed the redistribution of turbulent energy through Π_{ii}. The present results indicate that the stream-wise term Π_{11} is diminished compared to the 2DFPTBL case, though not as significantly as the production rate (Ölçmen and Simpson, 1996). With reduced near-wall redistribution from the stream-wise normal stress and nearly zero redistribution of the span-wise normal stress that is being produced, the near-wall vertical normal stress receives less energy from those co-planar components. As noted by Moin et al. (1990), the mechanisms that limit redistribution of

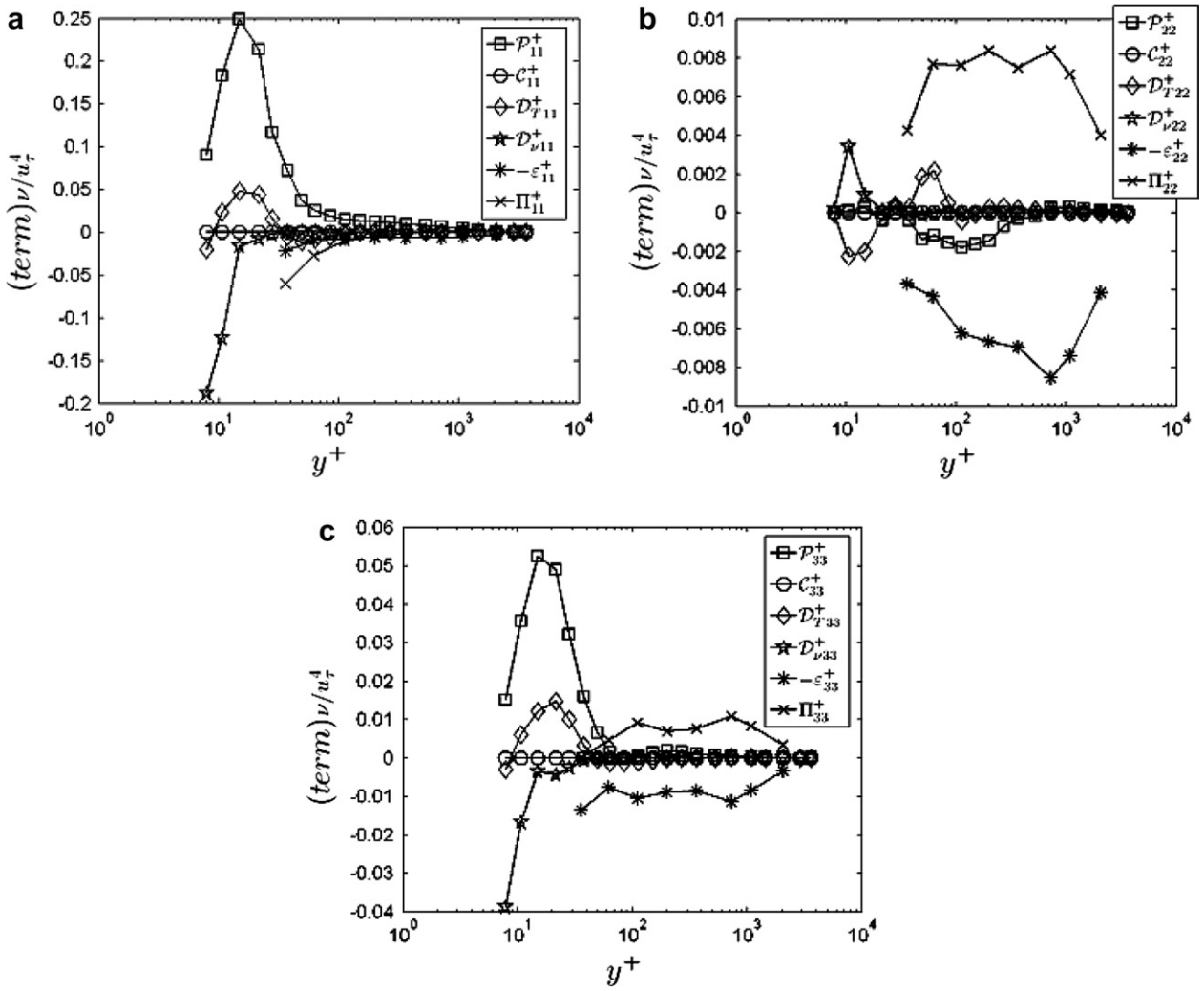

Fig. 14. Reynolds stress transport balances using the non-isotropic dissipation rates for the wing/body junction flow at station 5. (a) $\overline{u^2}^+$ (b) $\overline{v^2}^+$ (c) $\overline{w^2}^+$, P_{ij} = Production; C_{ij} = Convection; D_{vij} = Viscous diffusion; D_{Tij} = Turbulent diffusion; ϵ_{ij} = Dissipation rate; Π_{ij} = Velocity/pressure gradient correlation. Tunnel coordinate system.

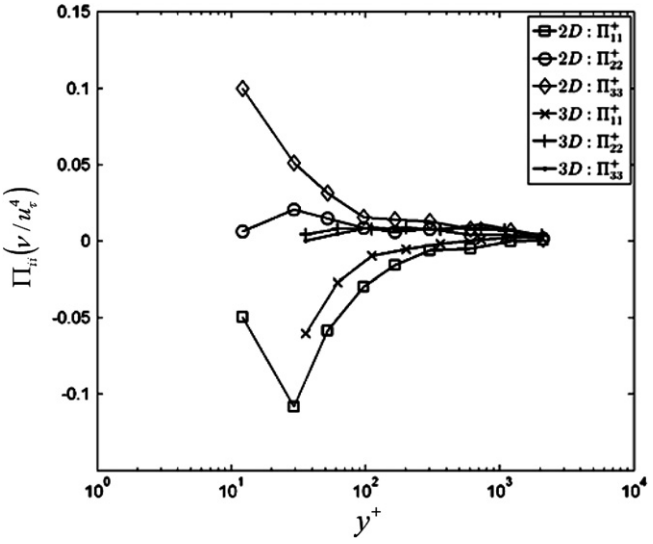

Fig. 15. Comparison of 2DFPTBL (2D) and 3D TBL (3D) results for Π_{ij}.

the normal stresses produced thereby reduce the transport of $\overline{v^2}$ and in turn diminish the production of turbulent shear stresses. The current data indicate a recovery of Π_{22} and Π_{33} to 2DFPTBL values above $y^+ = 300$, where $\overline{uv}$ shear stress levels reach approximately the same values as the 2DFPTBL (see Fig. 13 and Ölçmen and Simpson, 1996).

4. Conclusions

A novel experimental technique is reported for obtaining velocity gradients using highly resolved particle trajectory data in turbulent boundary layer flows. Results for non-isotropic dissipation rates in 2D and 3D turbulent boundary layers have been obtained. For the 2DFPTBL at $Re_\theta = 7500$, the dissipation rate is anisotropic to approximately the same viscous wall heights as in DNS for $Re_\theta = 1410$. Measurements of the velocity/pressure-gradient correlation have been obtained in a 3D TBL in the vicinity of a wing/body junction. As in the 2DFPTBL, much of the transport profiles for the span-wise and vertical normal stresses are dominated by the dissipation rate and velocity/pressure gradient correlations. The results indicate a magnitude reduction in the velocity/pressure-gradient correlation in the near-wall region for each of the Reynolds normal stresses. These results corroborate the DNS results of Moin et al. (1990), that reduced energy redistribution contributes to reduced shear stress magnitudes frequently observed in an variety of 3D TBLs.

Acknowledgements

This work was accomplished at the Virginia Tech Department of Aerospace and Ocean Engineering. The authors are grateful for the support provided by the National Science Foundation through grant CTS-0233653 under program manager Dr. Michael Plesniak and the Air Force Office of Scientific Research grant F49620-03-1-0057 under program manager Dr. Thomas Beutner.

References

Agui, J.H., Andreopoulos, Y., 2002. A new laser vorticity probe-LAVOR: its development and validation in turbulent boundary layer. Exp. Fluids 34 (2), 192–205.

Ahn, S., Simpson, R.L., 1987. Convective wave speed and spectral features of turbulent boundary layers. In: AIAA 25th Aerospace Sciences Meeting, Paper AIAA-87-0198, January 12–15, Reno, NV.

Albrecht, H.-E., Borys, M., Damaschke, N., Tropea, C., 2003. Laser Doppler and Phase Doppler Measurement Techniques. Springer-Verlag, New York.

Coleman, G.N., Kim, J., Spalart, P.R., 2000. A numerical study of strained three-dimensional wall-bounded turbulence. J. Fluid Mech. 416, 75–116.

Czarske, J., 2001. Laser–Doppler velocity profile sensor using a chromatic coding. Measur. Sci. Tech. 12, 52–57.

Czarske, J., Büttner, L., Razik, T., 2002. Boundary layer velocity measurements by a laser–Doppler profile sensor with micrometre spatial resolution. Measur. Sci. Tech. 13, 1979–1989.

DeGraaff, D.B., Eaton, J.K., 2000. Reynolds-number scaling of the flat-plate turbulent boundary layer. J. Fluid Mech. 422, 319–346.

Devenport, W.J., Simpson, R.L., 1990. Time-dependent and time-averaged turbulence structure near the nose of a wing–body junction. J. Fluid Mech. 210, 23–55.

Durst, F., Jovanovic', J., Sender, J., 1995. LDA measurements in the near wall region of a turbulent pipe flow. J. Fluid Mech. 295, 305.

Eaton, J.K., 1995. Effects of mean flow three dimensionality on turbulent boundary-layer structure. AIAA J. 31 (11), 2020–2025.

Hallbäck, M., Groth, J., Johansson, A.V., 1990. An algebraic model for non-isotropic turbulent dissipation rate in Reynolds stress closure. Phys. Fluids 2 (10), 1859–1866.

Labourasse, E., Sagaut, P., 2002. Reconstruction of turbulent fluctuations using a hybrid RANS/LES approach. J. Comput. Phys. 182 (1), 301–336.

Lai, Y.G., So, R.M.C., 1990. On near-wall turbulent flow modelling. J. Fluid Mech. 221, 641–673.

Lehmann, B., Nobach, H., Tropea, C., 2002. Measurement of acceleration using the laser–Doppler technique. Measur. Sci. Tech. 9, 1367–1381.

Lowe, K.T., 2006. Design and application of a novel laser–Doppler velocimeter for turbulence structural measurements in turbulent boundary layers, Ph.D. Dissertation, Department of Aerospace and Ocean Engr., Virginia Tech.

Lowe, K.T., Simpson, R.L., 2006. Measurements of velocity–acceleration statistics in turbulent boundary layers. Int. J. Heat Fluid Flow 27 (4), 558–565.

Lowe, K.T., Simpson, R.L., 2007. Doppler chirp signal processing for particle acceleration measurement with laser–Doppler velocimetry. In: Proceedings of the 14th Coherent Laser Radar. Conf., Snowmass, CO, USA.

Lowe, K.T., Simpson, R.L., in preparation. An advanced laser–Doppler velocimeter for three-component particle trajectory measurements, Measur. Sci. Tech.

Meneveau, C., Katz, J., 2000. Scale-invariance and turbulence models for large-eddy simulation. Annu. Rev. Fluid Mech. 32, 1–32.

Moin, P., Shih, T.-H., Driver, D., Mansour, N.N., 1990. Direct numerical simulation of a three-dimensional turbulent boundary layer. Phys. Fluids A 2 (10), 1846–1853.

Mullin, J.A., Dahm, W.J.A., 2006. Dual-plane stereo particle image velocimetry measurements of velocity gradient tensor fields in turbulent shear flow. I. Accuracy assessments. Phys. Fluids 18, 035101-1–035101-18.

Ölçmen, M.S., Simpson, R.L., 1995. An experimental study of a three-dimensional pressure-driven turbulent boundary layer. J. Fluid Mech. 290, 225–262.

Ölçmen, M.S., Simpson, R.L., 1996. Experimental transport-rate budgets in complex 3-D turbulent flow near a wing–body junction. In: 27th AIAA Fluid Mech. Conf., 17–20 June, New Orleans, LA, USA, Paper 96-2035.

Robinson, S.K., 1991. Coherent motions in the turbulent boundary layer. Annu. Rev. Fluid Mech. 23, 601–639.

Rotta, J.C., 1962. Turbulent boundary layers in incompressible flow. In: Ferri, A., Küchemann, D., Sterne, L.H.G. (Eds.), Prog. in Aeronautical Sciences, Vol. 2, Pergamon Press, Oxford, pp. 1–220.

Saddoughi, S.G., Veeravalli, S.V., 1994. Local isotropy in turbulent boundary layers at high Reynolds number. J. Fluid Mech. 268, 333–372.

Shinpaugh, K.A., Simpson, R.L., Wicks, A.L., Ha, S.M., Fleming, J.L., 1992. Signal-processing techniques for low signal-to-noise ratio laser–Doppler velocimetry signals. Exp. Fluids 12, 319–328.

Simpson, R.L., 2001. Junction flows. Annu. Rev. Fluid Mech. 33, 415–443.

Simpson, R.L., 2005. Some observations on the structure and modeling of 3-D turbulent boundary layers. TSFP-5, vol. 1, 27–29 June, Williamsburg, VA, USA, pp. 1–10.

Spalart, P., 1988. Direct simulation of a turbulent boundary layer up to $Re_\theta = 1410$. J. Fluid Mech. 187, 61–98.

Tang, G., 2004. Measurements of the tip-gap turbulent flow structure in a low-speed compressor cascade, Ph.D. Dissertation, Department of Aerospace and Ocean Engr., Virginia Tech.

Tarau, T., Stepaniuk, V.P., Otugen, M.V., 2002. Evaluation of a new laser gradient probe. In: 40th Annual AIAA Aerospace Sciences Meeting and Exhibit, January 14–17, Reno, NV, AIAA 2002-0688.

Wallace, J.M., Foss, J.F., 1995. The measurement of vorticity in turbulent flows. Annu. Rev. Fluid Mech. 27, 469–514.

Yao, S., Tong, P., Ackerson, B.J., 2001. Proposal and testing for a fiber-optic-based measurement of flow vorticity. Appl. Opt. 40 (24), 4022–4027.